Stress-controlled carbon diffusion channeling in bct-iron: A mean-field theory

Philippe Maugis, Sara Chentouf, Damien Connétable

Stress-controlled carbon diffusion channeling in bct-iron: A mean-field theory

P. Maugis [a, *], S. Chentouf [a], D. Connétable [b]

[a] Aix Marseille Univ, CNRS, IM2NP, Marseille, France
[b] CIRIMAT, CNRS-INP-UPS, ENSIACET, Toulouse, France

ARTICLE INFO

Keywords:
Metals and alloys
Anisotropy
Diffusion
Elasticity
Order-disorder effects
Computer simulations

ABSTRACT

Diffusion of interstitial carbon atoms in iron is the rate-limiting phenomenon of a number of phase transitions in body-centered (bcc) and body-centered tetragonal (bct) phases such as ferrite and martensite. These phases being rarely stress-free and undeformed, the influence of stress/strain on the diffusivity of carbon is essential, although scarcely documented. We developed a model of carbon elastodiffusion in bct-iron. We combined anisotropic linear elasticity theory of point defects, the dilute approximation of regular solutions and the multisite model of random walk into a coherent mean-field theory. The model allows predicting the effects of composition, temperature and mechanical loading on the anisotropy of carbon diffusion. Density functional theory calculations have provided most of the materials parameters. The predictions were successfully tested against kinetic Monte Carlo simulations. Our results show that compression of the crystal increases carbon diffusivity, while tension has the opposite effect. Axial straining is accompanied by a large anisotropy of diffusion. This effect could be exploited to produce stress-controlled diffusion channeling for the engineering of anisotropic microstructures during thermal ageing of martensitic Fe-C alloys.

1. Introduction

Martensite and bainite, microstructural constituents of high-strength Fe-C alloys, share the body-centered tetragonal (bct) crystal structure. They are often described as tetragonally distorted bcc-iron [1,2]. Indeed, in carbon-supersaturated stress-free martensite, preferential occupation of one of the three octahedral sublattices by the carbon atoms results in the symmetry breaking of the cubic host lattice into a variant of tetragonal crystal. Zener [3] was the first to propose that this long-range ordering is driven by the reduction in carbon-induced strain energy. Accordingly, thermodynamic equilibration may produce an order – disorder transition, leading to partially ordered bct-iron. In practical situations, however, a crystal variant is subjected to internal stresses (coherency stresses, dislocation stress fields, etc.) [4] and to externally applied stresses. These stresses add to the carbon-induced stresses and are likely to affect the degree of carbon ordering.

Ferrite, on the other hand, is usually defined as the low-carbon cubic phase. However, a ferrite crystal submitted to an axial stress, *e.g.* along <001>, deforms into a tetragonal crystal. This is why ferrite and martensite pertain to the same "phase region" [5]: they are two instances of bct-iron in the Fe-C-stress phase diagram. They differ only by their degree of long-range order: ferrite is the low-order, low-tetragonality instance while martensite is the high-order, high-tetragonality one [6].

Various models of order-disorder transition during low-temperature ageing [7–11] or severe plastic deformation [12,13] have been proposed in the literature. Some of them include the effect of particular mechanical loadings [7,14,15]. None includes a comprehensive study of the effects of tensile and compressive stress, neither do they fully treat the ferrite – martensite ordering transition under applied stress.

The first stages of low-temperature ageing of carbon-supersaturated iron (ordering, clustering and spinodal decomposition) involve carbon diffusion in the crystal lattice [16]. Unfortunately, carbon diffusivity in supersaturated iron is difficult to measure because of the instability of the solid solution. For this reason, only indirect evaluations have been performed [17,18]. The scarce measurements of the effect of pressure on carbon diffusivity are also indirect and unprecise [19,20]. Migration of carbon atoms in the lattice occurs by successive jumps from octahedral to first-

* Corresponding author.
E-mail address: philippe.maugis@im2np.fr (P. Maugis).

https://doi.org/10.1016/j.jallcom.2018.08.060

nearest-neighbor octahedral sites via saddle-point tetrahedral sites [21]. Hillert suggested that diffusion in martensite is impaired by the trapping of most carbon atoms in the energetically favored crystal sites [22]. This mechanism was confirmed by recent Molecular Dynamics (MD) simulations with an EAM potential [11]. However, to date a model of carbon diffusivity in martensite is lacking, and the effect of stress and partial ordering on the anisotropy of diffusion is not documented.

The purpose of this paper is to provide a quantitative model of carbon diffusion in bct-iron as function of carbon content, temperature and mechanical loading. The effect of an external strain or stress field is presented in the case of tetragonal crystal symmetry. Via modelling of the degree of ordering, ferrite and martensite are both treated in a coherent approach. Fe-C alloy thermodynamics is described by a mean-field elastochemical model based on the anisotropic elasticity theory of point defects and the dilute approximation of regular solutions [6]. Carbon diffusivity is derived from the thermally activated jump frequencies by using the multisite method [23,24]. Most material parameters of the model were calculated by density functional theory (DFT) calculations. Kinetic Monte Carlo (KMC) simulations have been used to test the predictions of the analytical formulae.

The next section of the paper describes the modelling methods and parameters. It starts with the order-disorder transition, follows with the carbon jump frequencies and diffusivities; it briefly presents the Monte Carlo and DFT set-ups. Results for tracer diffusion and diffusion in supersaturated bct-iron are presented in Secs. 3 and 4. Cases of fixed strain field and fixed stress field are distinguished. The results are compared to the literature in Sec. 5. The possibility of controlling diffusion anisotropy for microstructure design is discussed.

2. Modelling methods and parameters

2.1. Order-disorder transition

Thermodynamics of the Zener ordering in mechanically loaded bct-iron has been recently described within an elastochemical mean-field theory [6]. The model is based on the continuum elasticity theory of point defects coupled with the thermodynamics of dilute solid solutions. It relies on two main hypotheses:

- The material parameters (dipole tensor, stiffness tensor) are composition- and temperature-independent in the range of 0–10 at.% C and 0–1000 K. This hypothesis of homogeneous elasticity is correct within an accuracy of about 10% [25,26];
- Hillert's [22] assumption that the strain induced by the population of carbon atoms is uniform in the crystal (the mean-field approximation). This was confirmed by previous studies [27,28].

We summarize in the following the main results of the elastochemical model that are useful to the present study. The details can be found in Ref. [6].

Distortion of the bcc lattice results in a loss of crystal symmetry such that the octahedral and tetrahedral interstitial sites differentiate into 3 sets each: O_x, O_y, O_z and T_x, T_y, T_z, also labelled O_i and T_i, $i = 1, 2$ or 3 (Fig. 1). For example, sites O_z and T_z are characterized by their axial direction z, and their transverse directions x and y. The octahedral sites are the stable positions for carbon atoms, whereas the tetrahedral sites are saddle point positions for carbon migration. Diffusion occurs via O-T-O-… chains of carbon jumps [21].

In the frame of the anisotropic elasticity theory of point defects, the dipole tensor quantifies the far-field stress induced by a point defect in an undeformed cubic crystal. An interstitial carbon atom in bcc-iron is thus characterized by its dipole tensor $\mathbf{P}^{O_i}$ or $\mathbf{P}^{T_i}$ ($i = 1$, 2 or 3), depending on its sitting site. Because the octahedral and tetrahedral sites have tetragonal symmetry, all tensors are diagonal and have only two independent components [29]. For example, $\mathbf{P}^{O_3}$ as components $P_{11} = P_{22} = P_a^O$ and $P_{33} = P_c^O$. Alternatively, the tensor of relaxation volume characterizes the carbon-induced distortion of the free crystal. It derives from the dipole tensor via the (symmetric) compliance tensor $\mathbf{S}$: $\mathbf{V}^O = \mathbf{S}\mathbf{P}^O$ and $\mathbf{V}^T = \mathbf{S}\mathbf{P}^T$. The relaxation volume of a carbon atom is the first invariant of $\mathbf{V}$: $V^O = \mathrm{tr}(\mathbf{V}^O) = (S_{11} + 2S_{12})(P_c^O + 2P_a^O)$, and equivalently for V^T.

Stiffness constants and dipole tensors were calculated ab initio in the framework of the density functional theory (DFT). Calculations were performed according to the computational details described in Ref. [26]. The defect elastic dipole tensors $\mathbf{P}^O$ and $\mathbf{P}^T$ were calculated with the residual stress method [30]. To correct for the periodic images of the carbon atom, the residual stress on the supercell was fitted with a parabolic function of the supercell inverse volume. The resulting tensor components are listed in Table 1.

Table 1
Independent material parameters used in the calculations.

a_0 (nm)	P_a^O (eV)	P_c^O (eV)	P_a^T (eV)	P_c^T (eV)	C_{11} (GPa)	C_{12} (GPa)	H_m^0 (eV)	ν_0 (THz)
0.2855	10.0	17.0	14.8	5.37	267	147	0.872	149

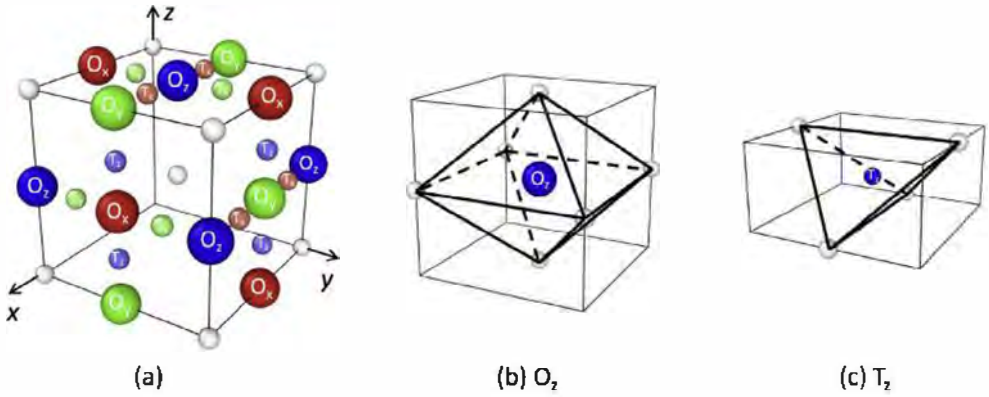

Fig. 1. (a) Body-centered orthorhombic cell. Iron atoms (white), octahedral interstitial sites (large colored spheres), and tetrahedral interstitial sites (small colored spheres). Red, green, blue colors refer to site types according to R = 1, G = 2, B = 3. (b) Octahedral z-site. (c) Tetrahedral z-site. (For interpretation of the references to color in this figure legend, the reader is referred to the Web version of this article.)

They are close to the values recently computed by DFT using different procedures [31]. As carbon atoms inserted in O or T sites induce lattice expansions in x, y and z directions, all components of $\mathbf{P}^{O}$ and $\mathbf{P}^{T}$ are positive. $\mathbf{P}^{O}$ is of prolate character, *i.e.* the singlet value is larger than the doublet value ($P_c^O > P_a^O$), whereas $\mathbf{P}^{T}$ is of oblate character ($P_c^O < P_a^O$). The implications of this will be examined in Secs. 3 and 4. For coherency, we adopted the stiffness coefficients calculated in the same conditions as the dipole tensors, although they differ by 15–20% from the experimental values [25]. The magnitude of this disparity is usually observed in metals. It will have no incidence on the calculated effects of an applied strain on the diffusivities. It will induce a relative error of the order of 1% on the calculated migration energies for an applied stress of 1000 MPa. The relative error on the calculated lattice parameters will be of the same order. These errors will have little influence on the general conclusions of the paper.

In the mean-field approximation, a configuration of carbon atoms in the crystal is defined by the atom fractions $c_i = n_i/n$, where n_i is the number of carbon atoms on the octahedral sites of type i, and n is the total number of iron atoms. The fraction $c = \sum c_i$ is the number of carbon atoms per iron atom in the crystal. We define the average dipole tensor $\mathbf{P}$ of the carbon atoms on octahedral sites, per iron atom, as $\mathbf{P} = \sum c_i \mathbf{P}^{O_i}$

Under applied strain, the site energies of the three sets of octahedral sites differ, leading to preferential occupation at equilibrium. The site energies of the tetrahedral sites also differ, affecting the diffusivity of carbon as function of temperature, composition and strain. For the equilibrium calculations, two cases must be distinguished, depending whether the strain tensor or the stress tensor is constrained to a constant value during transformations.

2.1.1. Case of fixed strain field

In this situation, the uniform strain tensor $\boldsymbol{\varepsilon}$ is applied to a crystal of volume $\mathscr{V}$. Thermodynamic equilibrium is reached when the Helmholtz free energy $F = U - TS$ is extremal. From the elasticity theory of point defects [32,33] the energy per iron atom, as reference to the unstrained, cubic lattice, comprises a self-energy term and a carbon-strain interaction energy term:

$$U(\boldsymbol{\varepsilon}) = \frac{1}{2} V_0 \mathbf{C}\boldsymbol{\varepsilon} : \boldsymbol{\varepsilon} - \mathbf{P} : \boldsymbol{\varepsilon}. \tag{1}$$

In this equation, $V_0 = \frac{1}{2}a_0^3$ is the volume per iron atom of unstrained crystal, $\mathbf{C}$ is the stiffness tensor, $\boldsymbol{\varepsilon}$ is the applied strain tensor, and $\mathbf{P}$ is the average elastic dipole tensor of the octahedral defects, as defined above. At mechanical equilibrium, imposing the strain $\boldsymbol{\varepsilon}$ necessitates that a stress $\boldsymbol{\sigma} = (1/V_0)\mathrm{d}U/\mathrm{d}\boldsymbol{\varepsilon}$ be applied to the boundaries of the crystal, *i.e.*

$$\boldsymbol{\sigma} = \mathbf{C}\boldsymbol{\varepsilon} - \frac{\mathbf{P}}{V_0}. \tag{2}$$

2.1.2. Case of fixed applied stress

In practice, imposing a strain tensor to a solid is a difficult task. A more common situation is to apply a stress tensor $\boldsymbol{\sigma}$. In this case, mechanical equilibrium is reached when the enthalpy H is extremal. The enthalpy per iron atom has the form of a Legendre transformation of the energy function U:

$$H = \frac{1}{2} V_0 \mathbf{C}\boldsymbol{\varepsilon} : \boldsymbol{\varepsilon} - \mathbf{P} : \boldsymbol{\varepsilon} - V_0 \boldsymbol{\sigma} : \boldsymbol{\varepsilon}. \tag{3}$$

The condition $\mathrm{d}H/\mathrm{d}\boldsymbol{\varepsilon} = 0$ yields the strain at equilibrium

$$\boldsymbol{\varepsilon} = \mathbf{S}\left(\boldsymbol{\sigma} + \frac{\mathbf{P}}{V_0}\right), \tag{4}$$

where $\mathbf{S} = \mathbf{C}^{-1}$ is the compliance tensor. As expected from formal thermodynamics, Eq. (4) is equivalent to Eq. (2). It states that the equilibrium strain results from the carbon-induced internal stress $\mathbf{P}/V_0$ added to the applied stress $\boldsymbol{\sigma}$. The enthalpy function then writes

$$H(\boldsymbol{\sigma}) = -\frac{1}{2} V_0 \left(\boldsymbol{\sigma} + \frac{\mathbf{P}}{V_0}\right) : \mathbf{S}\left(\boldsymbol{\sigma} + \frac{\mathbf{P}}{V_0}\right). \tag{5}$$

To complete the thermodynamic description, the configurational entropy of ordering in the dilute limit is introduced. In the following, we will consider the case of a crystal variant submitted to a stress tensor of tetragonal symmetry, aligned with the z axis of the crystal. The elastochemical model allows predicting the degree of long-range order of carbon as function of composition, temperature and stress. The order parameter is defined as $\eta = (c_3 - c_{1\text{ or }2})/c$, the deviatoric stress is $\Sigma = \sigma_{33} - \sigma_{11}$ and the pressure is p. Thermodynamic equilibrium can be computed by searching for the order parameter that minimizes the Gibbs energy of ordering

$$\Delta G(\eta) = -h_\eta c^2 \eta^2 - 2V_\Sigma \Sigma c \eta + \frac{1}{3} k_B T c \begin{bmatrix} 2(1-\eta)\ln(1-\eta) \\ +(1+2\eta)\ln(1+2\eta) \end{bmatrix}, \tag{6}$$

with

$$\begin{aligned} V_\Sigma &= \frac{1}{3}(S_{11} - S_{12})\left(P_c^O - P_a^O\right), \\ h_\eta &= \frac{V_\Sigma}{V_0}\left(P_c^O - P_a^O\right). \end{aligned} \tag{7}$$

$3V_\Sigma$ is the deviatoric $V_{33} - V_{11}$ of the tensor of relaxation volume $\mathbf{V}^O$, and h_η is the strain-energy parameter. For a given order parameter η, the corresponding strains are

$$\begin{aligned} \varepsilon_{11} = \varepsilon_{22} &= \frac{1}{3}\left[-3(S_{11}+2S_{12})p - (S_{11}-S_{12})\Sigma + \frac{V^O}{V_0}c - 3\frac{V_\Sigma}{V_0}c\eta\right] \\ \varepsilon_{33} &= \frac{1}{3}\left[-3(S_{11}+2S_{12})p + 2(S_{11}-S_{12})\Sigma + \frac{V^O}{V_0}c + 6\frac{V_\Sigma}{V_0}c\eta\right] \end{aligned} \tag{8}$$

The composition – stress diagram computed at room temperature from Eqs. (6)–(7) and the data of Table 1 is presented in Fig. 2.

Ferrite and martensite are respectively the low-order and high-order instances of bct-iron. Coexistence of both phases occurs along the $\Sigma(c)$ curve (solid line in Fig. 2). The curve ends at the critical point, beyond which spreads the domain of *supercritical bct-iron*. The arcs indicate the stability domains of prolate (axial ratio $c/a > 1$, $\eta > 0$) and oblate ($c/a < 1$, $\eta < 0$) tetragonality. Cubic ferrite ($\eta = 0$) is stable only under hydrostatic pressure, *i.e.* at $\Sigma = 0$ (horizontal segment in Fig. 2). Numerically, the critical point lies at $c_K = 0.0120$ (0.27 wt%) and $\Sigma_K = 11.5$ MPa. The ferrite – martensite transition under zero stress occurs at $c_0 = 0.0125$ (0.25 wt%). This value is in the range of 0.20 wt% to 0.6 wt% reported in the literature [10,34,35].

2.2. Jump frequencies

Let's consider a carbon atom on an octahedral site O_i migrating

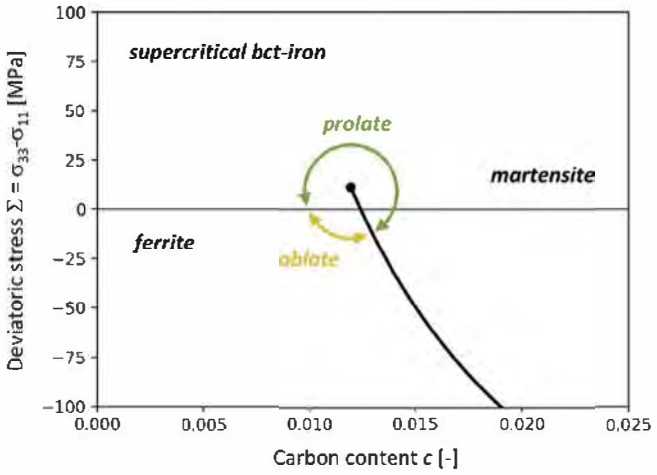

Fig. 2. Composition − stress diagram computed at $T = 293$ K. The critical point has coordinates $c_K = 0.0120$ and $\Sigma_K = 11.5$ MPa (black point).

towards a first-neighbor octahedral site O_k via the saddle-point tetrahedral site T_j ($i \neq j \neq k$). During the jump, under fixed strain, the crystal has to overcome an energy barrier E_{ij}. According to the rate theory, the jump frequency related to this particular jump is $\Gamma_{ij} = \nu_0 \exp(-E_{ij}/k_B T)$. The attempt frequency ν_0 is assumed strain-independent. Through E_{ij}, the strain-dependence of the site energies E^O and E^T is the origin of the strain effect on carbon diffusivity and diffusion anisotropy. A similar reasoning explains the stress effect, via the stress-dependent migration enthalpy. In the following, we will distinguish the fixed-strain and fixed-stress conditions.

2.2.1. Migration under fixed strain

We define the interstitial site energy $E^{O\text{ or }T}$ as the change in crystal energy upon inserting a carbon atom in O or T position under fixed strain: the site energy is the energetic part of the chemical potential of carbon. The elastic energy changes upon carbon addition because the total dipole tensor of the crystal is modified by the amount $\mathbf{P}^{O\text{ or }T}$ in the process. From Eq. (1) we have

$$E^{O\text{ or }T} = E_0^{O\text{ or }T} - \mathbf{P}^{O\text{ or }T} : \boldsymbol{\varepsilon}. \tag{9}$$

$E_0^{O\text{ or }T}$ is the site energy in the undeformed cubic crystal. The term $-\mathbf{P}^{O\text{ or }T} : \boldsymbol{\varepsilon}$ is the interaction energy of the carbon atom with the strain field. This energy is minimum when the scalar product $\mathbf{P}^{O\text{ or }T} : \boldsymbol{\varepsilon}$ is maximum. The case of uniaxial strain field along z, with $\boldsymbol{\varepsilon} = (0, 0, \varepsilon_0)$ is simple: (i) an O site verifies $P_c^O > P_a^O$ (see Table 1), thus traction ($\varepsilon_0 > 0$) favors O_z sites, while compression ($\varepsilon_0 < 0$) equally favors O_x and O_y sites compared to O_z. This is the origin of strain-induced Zener ordering and inverse-Zener ordering [6,15]. (ii) On the contrary, a T site has $P_c^T < P_a^T$: traction favors T_x and T_y sites compared to T_z, and the opposite for compression.

The migration energy E^m is the difference in site energies $E^T - E^O$. From Eq. (9),

$$E^m = E_0^m - \left(\mathbf{P}^T - \mathbf{P}^O\right) : \boldsymbol{\varepsilon}. \tag{10}$$

$E_0^m = E_0^T - E_0^O$ is the migration energy in the undeformed crystal. For a given jump, the dipole tensor of migration $\Delta\mathbf{P} = \mathbf{P}^T - \mathbf{P}^O$ governs the influence of strain on the migration energy for the jump. $\mathbf{P}^O$ and $\mathbf{P}^T$ have tetragonal symmetry but the combination $\mathbf{P}^T - \mathbf{P}^O$ breaks the original symmetries into orthorhombic symmetry; hence $\Delta\mathbf{P}$ has three distinct components. They are at the origin of the anisotropy of diffusion, as will be shown in Sec. 3.

2.2.2. Migration under fixed stress

In the case of fixed stress, we consider the migration enthalpy H^m. The elastic effect on the migration enthalpy originates from both the change in total dipole tensor and the change in crystal strain during a jump. From Eq. (5),

$$H^m = H_0^m - \mathbf{S}\left(\mathbf{P}^T - \mathbf{P}^O\right) : \left(\boldsymbol{\sigma} + \frac{\mathbf{P}}{V_0}\right) - \frac{1}{2}\left(\mathbf{P}^T - \mathbf{P}^O\right) : \left(\boldsymbol{\varepsilon}^T - \boldsymbol{\varepsilon}^O\right). \tag{11}$$

Strains $\boldsymbol{\varepsilon}^O = \mathbf{S}\mathbf{P}^O / \mathscr{V}$ and $\boldsymbol{\varepsilon}^T = \mathbf{S}\mathbf{P}^T / \mathscr{V}$ are the deformations of a relaxed crystal of volume $\mathscr{V}$ induced by one carbon atom in respectively O and T positions. It is only significant for nanocrystals. In the limit of large crystals, we will use the simplified form

$$H^m = H_0^m - \mathbf{S}\left(\mathbf{P}^T - \mathbf{P}^O\right) : \left(\boldsymbol{\sigma} + \frac{\mathbf{P}}{V_0}\right). \tag{12}$$

This formula involves the tensor of activation volume of the jump $\Delta\mathbf{V} = \mathbf{S}(\mathbf{P}^T - \mathbf{P}^O)$. In the case of pure ferrite under pressure p, $\mathbf{P}$ vanishes, and the enthalpy of migration takes the usual form $H^m = H_0^m - p\Delta V$, where $\Delta V = V^T - V^O$ is the activation volume. Since $\mathbf{S}(\boldsymbol{\sigma} + \mathbf{P}/V_0)$ is the strain tensor $\boldsymbol{\varepsilon}$, Eq. (12) and Eq. (10) have the same form, and consequently $H_0^m = E_0^m$.

2.3. Diffusivities

We restricted our study to tetragonal crystals. Even in these case, the effect of the migration energies on the diffusivity is not straightforward because three different types of jumps are involved. To derive the analytic form of the diffusivities, we used an approach similar to that described in the paper of David et al. [36], which uses the multisite method developed by Landman et al. [24]. The diffusivities then write

$$D_x = D_y = \frac{a_x^2}{2}\frac{\Gamma_{31}\Gamma_{12}}{2\Gamma_{31} + \Gamma_{12}}, \tag{13}$$

and

$$D_z = \frac{a_z^2}{2}\frac{\Gamma_{31}\Gamma_{13}}{2\Gamma_{31} + \Gamma_{12}}. \tag{14}$$

a_x and a_z are the transverse and axial lattice parameters of the quadratic unit cell. When the structure is cubic, $a_x = a_z = a$, $\Gamma_{12} = \Gamma_{13} = \Gamma_{31} = \Gamma$, and one recovers the classical formula $D = \Gamma a^2/6$ [37]. In the numerical evaluations, we neglected the variations in lattice parameters and set $a_x = a_z = a_0$. The ratio D_z/D_x quantifies the anisotropy of diffusion:

$$\frac{D_z}{D_x} = \left(\frac{a_z}{a_x}\right)^2 \frac{\Gamma_{13}}{\Gamma_{12}}. \tag{15}$$

Experimental data of tracer diffusion in stress-free ferrite were used to fit the attempt frequency ν_0 and migration enthalpy H_0^m: The isotropic diffusivity of carbon writes [37]

$$D = D_0 \exp\left(-\frac{H_0^m}{k_B T}\right) \tag{16}$$

with

$$D_0 = \frac{Z}{6}\lambda^2 \nu_0. \tag{17}$$

The coordinance is $Z = 4$ and jump length is $\lambda = a_0/2$.

Either experimental data or calculated data of tracer diffusion in stress-free ferrite can be used to fit the values of D_0 and H_0^m. Our calculations were performed using the Vienna ab initio simulation package (VASP) [38]. Self-consistent Kohn-Sham equations were solved using the projector augmented wave (PAW) pseudo-potentials [39]. The Perdew-Burke-Ernzerhof (PBE [40]) exchange and correlation functional was used. The plane-wave energy cut-off was set to 400 eV and Γ-centered Monkhorst-Pack meshes [41] were used to sample the first Brillouin zone (equivalent to $48 \times 48 \times 48$ for the primitive cell). For site energy calculations, a supercell approach ($3 \times 3 \times 3$ cubic cells, i.e. 54 Fe atoms) was used with periodic boundary conditions to describe systems with and without point defect. Atomic positions and lattice parameters (shapes and volumes) were fully relaxed. Simulations were performed with spin polarization to model the ferromagnetic state of iron. Vibrational properties and inter-atomic force constants (IFCs) were obtained as finite differences of forces with respect to atomic displacements fields. Due to an excessive numerical cost, IFCs were only conducted on primitive $3 \times 3 \times 3$ supercells, i.e. with 27 Fe atoms. The phonopy package [42] was used to generate finite displacements according to the symmetry of each structure. In all cases discussed here, the full inter-atomic vibrational forces of the supercells were computed, for stable and transition states.

The jump frequency $\Gamma = \nu_0 \exp(-H_0^m/k_B T)$ was computed from the transition rate theory [43], by using

$$\nu_0(T) = \frac{k_B T}{h} \frac{\mathcal{Z}_{TS}}{\mathcal{Z}_I}, \tag{18}$$

where $\mathcal{Z}_{TS}$ and $\mathcal{Z}_I$ are the partition functions for the transition state (tetrahedral site) and the initial state (octahedral site) respectively. $\mathcal{Z}$ is related to the vibration frequencies $\omega_{\boldsymbol{q}\nu}$ of the system:

$$\ln \mathcal{Z} = -\sum_{\boldsymbol{q}\nu} \ln\left[2\sinh\left(-\frac{\hbar\omega_{\boldsymbol{q}\nu}}{2k_B T}\right)\right] \tag{19}$$

The calculated value of ν_0 from Eqs. (18) and (19) is a slowly varying function of temperature. Fitting the calculated diffusivity in the range of 235–1000 K yields $H_0^m = 0.888$ eV and $D_0 = 3.51 \times 10^{-7}$ m^2/s. These values are in the range of the previous theoretical calculations and coincide with the low-temperature experimental data [44].

In order to predict to a good accuracy the effect of stresses on diffusivity in the widest range of temperature, we preferred to rely on the fit of the experimental data collected by da Silva et al. [45]: $H_0^m = 0.872$ eV and $D_0 = 2 \times 10^{-6}$ m^2/s. Identification to Eq. (17) yields $\nu_0 = 149$ THz. These values are identical to the ones used by Gendt et al. [46] and Hin et al. [47,48] in their KMC simulations. According to these data, carbon atoms jump at room-temperature (293 K) in pure cubic ferrite at the frequency $\Gamma = 0.15$ Hz, corresponding to the diffusivity $D = 2.03 \times 10^{-21}$ m^2/s.

2.4. Kinetic Monte Carlo simulations

Kinetic Monte Carlo simulations were performed on the rigid lattice of the octahedral sites. This cubic lattice is the reference frame for the linear elasticity calculations. Periodic boundary conditions were applied to the simulation box. The average residence-time algorithm was used to provide the correct time-scale [49]. Calculations in dilute ferrite were carried out in a box of $8 \times 8 \times 8$ cells containing one carbon atom, performing 10^6 successive jumps, corresponding to a root-mean-square (RMS) displacement of around 1450 Å. For calculations in supersaturated iron, a total of ~1600 carbon atoms were inserted, and the box size was adjusted in relation to the carbon content. To compute de diffusion coefficients, each carbon atom was allowed an average of 45 jumps, corresponding to a RMS displacement of ~9 Å. The RMS displacement was averaged over all carbon atoms in the simulation box. With these settings, the relative convergence on the diffusivities was better than 1%.

The diffusivities D_x, D_y, D_z are related to the displacements R_x, R_y and R_z along x, y and z directions, via Einstein's equation:

$$R_x^2 = 2D_x t,\ R_y^2 = 2D_y t \text{ and } R_z^2 = 2D_z t. \tag{20}$$

The total diffusivity is

$$D = \frac{1}{3}(D_x + D_y + D_z). \tag{21}$$

The successive carbon jumps being uncorrelated, R_x^2 is calculated as the sum of the squares of jump lengths $\sum (\Delta x)^2$ over the simulation time. Idem for R_y^2 and R_z^2.

3. Tracer diffusion in dilute bct-iron

At infinite dilution, the deformation induced by the carbon atoms is vanishing. The total stress reduces to the applied stress, which can be controlled via an applied strain. We considered specific cases of applied strain: uniaxial, biaxial and isotropic traction and compression. The results of the KMC simulations are compared to the model of elastodiffusion, and discussed.

3.1. Results of Monte Carlo simulations

Fig. 3 shows the positions occupied by one carbon atom during a run of 300 jumps at room temperature. Three cases are presented: (a) The absence of strain insured isotropic diffusion. (b) 5% axial expansion along z induced diffusion anisotropy, all displacements occurring in a transverse x-y plane. (c) 5% axial contraction along z induced *diffusion channeling* along the z axis.

Table 2 summarizes the calculated diffusivities for various strain tensors. The applied strain produced acceleration or slow-down, isotropic, transverse, or axial diffusion depending on the components of the strain tensor.

KMC simulations agree with the analytical model within a relative accuracy better than 1%, confirming the coherency of our approach. This allows using the mathematical formulae [Eqs. (13) and (14)] to interpret the numerical results and trends in the diffusion behavior.

3.2. Interpretation of the diffusion behavior

3.2.1. Migration energies

The tetragonal distortion of the bcc cell breaks the octahedral sites into two sets of non-equivalent sites: $O_x \equiv O_y$ and O_z. The same occurs for the tetrahedral sites. As a result, the strain-induced migration energy $E_{ij} = E_0^m - (\mathbf{P}^{T_j} - \mathbf{P}^{O_i}) : \boldsymbol{\varepsilon}$ can take three distinct values: $E_{12} = E_{21}$, $E_{13} = E_{23}$, and $E_{31} = E_{32}$ (see Fig. 1a). To split up the effect of the applied strain into isotropic and deviatoric terms, we introduce the volume expansion $\mathrm{tr}\boldsymbol{\varepsilon} = \Delta V/V_0$ and the deviatoric strain $\in = \varepsilon_{33} - \varepsilon_{11}$. The migration energies then write

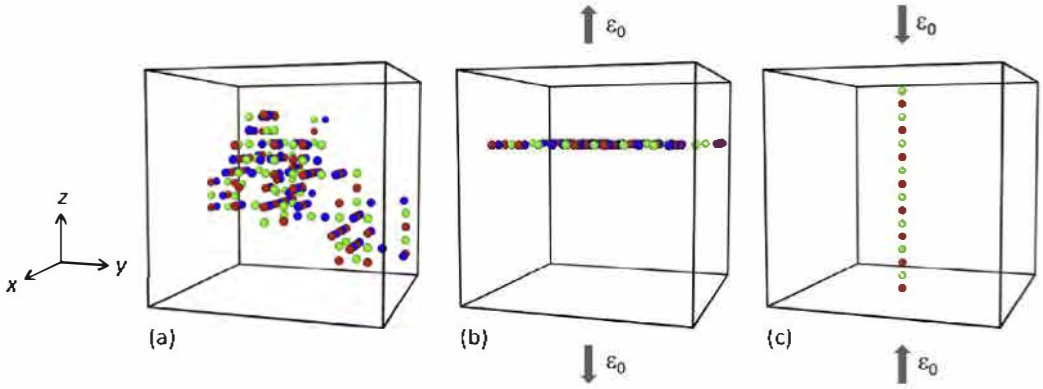

Fig. 3. 300 successive carbon positions during diffusion at 293 K. (a) isotropic diffusion, $\boldsymbol{\varepsilon} = (0, 0, 0)$, (b) x-y transverse anisotropy, $\boldsymbol{\varepsilon} = (0, 0, 0.05)$, and (c) z-channeling, $\boldsymbol{\varepsilon} = (0, 0, -0.05)$.

Table 2
Effect of an applied strain ($\varepsilon_{11}, \varepsilon_{22}, \varepsilon_{33}$) on the diffusivities D_x, D_y, D_z and D (in m^2/s) at room temperature ($T = 293$ K).

ε_{11}	ε_{22}	ε_{33}	$D_x = D_y$	D_z	D	D_z/D_x
0	0	0	2.03×10^{-21}	2.03×10^{-21}	2.03×10^{-21}	1
0.01	0.01	0.01	9.07×10^{-22}	9.07×10^{-22}	9.07×10^{-22}	1
−0.01	−0.01	−0.01	4.53×10^{-21}	4.53×10^{-21}	4.53×10^{-21}	1
0	0	0.01	2.26×10^{-21}	5.41×10^{-23}	1.53×10^{-21}	0.024
0	0	−0.01	4.39×10^{-22}	1.85×10^{-20}	6.44×10^{-21}	42.
0.01	0.01	0	1.97×10^{-22}	8.26×10^{-21}	2.88×10^{-21}	42.
−0.01	−0.01	0	5.06×10^{-21}	1.21×10^{-22}	3.41×10^{-21}	0.024

$$
\begin{aligned}
E_{12} &= E_0^{\mathrm{m}} - \frac{1}{3}\left[\Delta P\,\mathrm{tr}\boldsymbol{\varepsilon} + \left(-P_c^{\mathrm{T}} + P_a^{\mathrm{T}} + P_c^{\mathrm{O}} - P_a^{\mathrm{O}}\right)\in\right] \\
E_{13} &= E_0^{\mathrm{m}} - \frac{1}{3}\left[\Delta P\,\mathrm{tr}\boldsymbol{\varepsilon} + \left(2P_c^{\mathrm{T}} - 2P_a^{\mathrm{T}} + P_c^{\mathrm{O}} - P_a^{\mathrm{O}}\right)\in\right] \\
E_{31} &= E_0^{\mathrm{m}} - \frac{1}{3}\left[\Delta P\,\mathrm{tr}\boldsymbol{\varepsilon} + \left(-P_c^{\mathrm{T}} + P_a^{\mathrm{T}} - 2P_c^{\mathrm{O}} + 2P_a^{\mathrm{O}}\right)\in\right]
\end{aligned}
\tag{22}
$$

with $\Delta P = \mathrm{tr}(\mathbf{P}^{\mathrm{T}} - \mathbf{P}^{\mathrm{O}})$. The effect of the volume expansion is identical for all three activation energies. Anisotropy arises from the deviatoric part the strain tensor, via linear combinations of $P_c^{\mathrm{O}} - P_a^{\mathrm{O}}$ and $P_c^{\mathrm{T}} - P_a^{\mathrm{T}}$, which represent the tetragonal anisotropy of the O and T interstitial sites. Three particular cases of strain symmetry are of interest:

1) Isotropic dilatation/contraction.
In this case, $\in = 0$. The three migration energies are equal to

$$E^{\mathrm{isotropic}} = E_0^{\mathrm{m}} - \frac{1}{3}\Delta P\,\mathrm{tr}\boldsymbol{\varepsilon}, \tag{23}$$

and diffusion is isotropic. With the data of Table 1, $\Delta P = -2.03$ eV, *i.e.* isotropic dilatation favors more the octahedral sites than the tetrahedral sites. Hence, lattice dilatation reduces the diffusivity, while lattice contraction increases it, as can be checked in Table 2.

2) Uniaxial strain.
With the strain tensor $\boldsymbol{\varepsilon} = (0, 0, \varepsilon_0)$ the three migration energies are written numerically (in eV):

$$
\begin{aligned}
E_{12}^{\mathrm{uniaxial}} &= 0.872 - 4.80\varepsilon_0 \\
E_{13}^{\mathrm{uniaxial}} &= 0.872 + 4.63\varepsilon_0 \\
E_{31}^{\mathrm{uniaxial}} &= 0.872 + 2.20\varepsilon_0
\end{aligned}
\tag{24}
$$

Fig. 4 exemplifies the corresponding energy paths of migration in a case of axial expansion ($\varepsilon_0 > 0$). O_3 sites are energetically favored sites for carbon compared to O_1 and O_2, while T_3 are energetically disfavored compared to T_1 and T_2. Consequently, the $O_1 \rightarrow T_2 \rightarrow O_3$ and $O_2 \rightarrow T_1 \rightarrow O_3$ transverse jumps have the lowest migration energy: expansion in direction z favors atomic jumps in the x-y plane. Meanwhile, the axial jumps $O_1 \rightarrow T_3 \rightarrow O_2$ and $O_2 \rightarrow T_3 \rightarrow O_1$ are the most disfavored. Hence, axial expansion produces transverse in-plane diffusion. On the opposite, axial contraction favors the axial jumps and produces axial diffusion, *i.e. channeling* of the carbon atoms along the contracted axis. This behavior is confirmed by the KMC results (see Table 2).

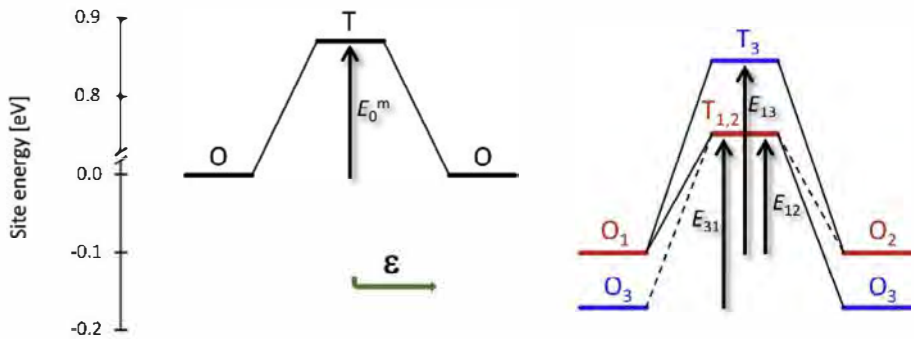

Fig. 4. Energy paths of carbon migration. Site energies and migration energy E_{ij} for a carbon jump from an octahedral site (O_i) to an octahedral site (O_k) via a tetrahedral site (T_j). Left: cubic cell $\boldsymbol{\varepsilon} = (0, 0, 0)$, right: tetragonal cell $\boldsymbol{\varepsilon} = (0, 0, 0.01)$. Axial expansion lowers E_{12} and favors x-y in-plane atomic jumps.

3) Biaxial strain.

With the strain tensor $\boldsymbol{\varepsilon} = (\varepsilon_0, \varepsilon_0, 0)$, the three migration energies write (in eV)

$$\begin{aligned} E_{12}^{\text{biaxial}} &= 0.872 + 6.83\varepsilon_0 \\ E_{13}^{\text{biaxial}} &= 0.872 - 2.60\varepsilon_0 \\ E_{31}^{\text{biaxial}} &= 0.872 - 0.17\varepsilon_0 \end{aligned} \tag{25}$$

According to these values, biaxial expansion ($\varepsilon_0 > 0$) produces z-channeling, while biaxial contraction ($\varepsilon_0 < 0$) produces x-y in-plane diffusion (see Table 2). In terms of anisotropy, the situation is analogous to the uniaxial case since the anisotropy of diffusion is a function of the deviatoric $\in$ of the strain only, and $\in(\varepsilon_0, \varepsilon_0, 0) = \in(0, 0, -\varepsilon_0) = -\varepsilon_0$: contraction along z is equivalent to expansion along x and y directions.

3.2.2. *Diffusivities*

In the case of tetragonal deformation, Eq. (15) gives the anisotropy ratio

$$\frac{D_z}{D_x} = \left(\frac{a_z}{a_x}\right)^2 \exp\left[-\frac{\left(P_a^T - P_c^T\right)\in}{k_B T}\right] \tag{26}$$

We will restrict our analysis to the case of uniaxial expansion/contraction. With the uniaxial strain $\boldsymbol{\varepsilon} = (0, 0, \varepsilon_0)$, the deviatoric strain is $\in = \varepsilon_0$. The anisotropy ratio [Eq. (26)] depends on the properties of the tetrahedral sites via the difference $P_a^T - P_c^T = 9.43$ eV. As this value is positive, we have $D_z < D_x$ when $\varepsilon_0 > 0$ and $D_z > D_x$ when $\varepsilon_0 < 0$. In addition, the ratio D_z/D_x is inversed when the strain changes sign. This behavior confirms our previous analysis of the jump frequencies. The effect of temperature on the anisotropy ratio also reverses when the strain changes sign. When the temperature increases the anisotropy tends asymptotically to 1. These conclusions are in qualitative agreement with the alternate approach of Trinkle [50].

Contrary to the migration energies E_{ij}, the diffusivities D_i are not symmetric about $\varepsilon_0 = 0$, as the slopes change around a positive strain (Fig. 5). The diffusivities are neither monotonous functions: at room temperature, D_x peaks at about $\varepsilon_0 = 0.005$. The axial and transverse diffusivities follow different slopes: *e.g.* D_x loses of factor of 25 over 5% of axial expansion, whereas D_z gains 4 orders of magnitude over 5% of axial contraction.

For large strain or low temperature, one among the three types of atomic jumps dictates the diffusional behavior:

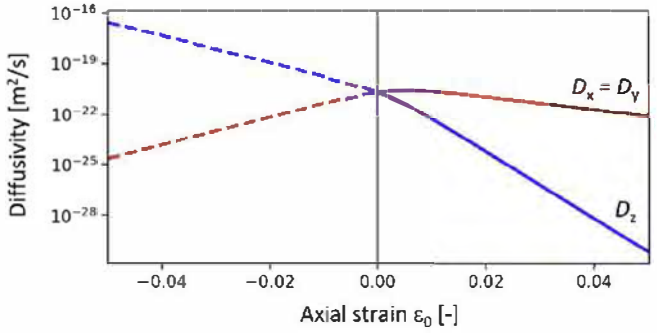

Fig. 5. Effect of an axial strain $\boldsymbol{\varepsilon} = (0, 0, \varepsilon_0)$ on diffusivities at $T = 293$ K. Axial expansion promotes transverse diffusion, whereas contraction promotes axial diffusion channeling. Cubic ferrite is at abscissa $\varepsilon_0 = 0$.

1) In the case of uniaxial expansion, Γ_{12} is the major frequency, due to its smallest migration energy [Eq. (24)]. Transverse diffusion occurs in the x-y plane since $D_z \ll D_x, D_y$ [Eqs. (13) and (14)]. The total diffusivity simplifies into $D \approx \frac{2}{3}(a_x^2/2)\Gamma_{31}$. Diffusion proceeds by successive carbon jumps in a x-y plane along the chain $O_{1\text{ or }2} \rightarrow O_3 \rightarrow O_{1\text{ or }2} \rightarrow O_3 \ldots$ (see Fig. 3). The rate-limiting step in the chain is the jump out of the trapping site O_3, towards x or y direction. The activation energy for diffusion is $E_{31} = 0.872 + 2.20\varepsilon_0$.
2) In the case of uniaxial contraction, Γ_{13} is the major frequency and $\Gamma_{31} \gg \Gamma_{12}$. Channeling occurs along the z axis ($D_z \gg D_x, D_y$). The diffusivity is $D \approx \frac{1}{3}(a_z^2/2)\Gamma_{13}$. Diffusion proceeds by successive jumps in a z axis along the chain $O_1 \rightarrow O_2 \rightarrow O_1 \ldots$ avoiding the disfavored sites of type 3 (see Fig. 3). The activation energy for diffusion is $E_{13} = 0.872 + 4.63\varepsilon_0$.

Comparing cases 1 and 2, the effect of axial contraction on the activation energy for diffusion is twice larger than the effect of axial expansion. Arrhenius laws for the two cases are depicted in Fig. 6. Under compressive strain, the diffusivity is higher, and decreases less steeply with temperature decrease than under tractional strain.

As a partial conclusion, we showed that lattice strain affects the magnitude of carbon diffusivity, which can be largely increased or decreased. Axial strain induces axial channeling or transverse diffusion, depending on its sign. This behavior can be rationalized via the strain-induced changes in migration energies coupled to the formulae of the anisotropic diffusivities. These findings will serve as a basis for understanding the effect of stress in supersaturated bct-iron, as will be shown in the next section.

4. Diffusion in supersaturated bct-iron

In a supersaturated crystal, carbon atoms contribute to the total strain of the crystal, in addition to the external stress. Then, from Sec. 3, we expect that carbon content and the degree of long-range carbon ordering affect the diffusivities. Considering the case of fixed-stress transformations, the diffusivities were computed as follows: for a given composition, temperature and stress tensor, the equilibrium degree of order was computed via minimization of the Gibbs energy of ordering (Eq. (6)). Each degree of ordering corresponds to an average dipole tensor, from which the migration enthalpies (Eq. (12)) and the resulting diffusivities (Eqs. (13) and (14))

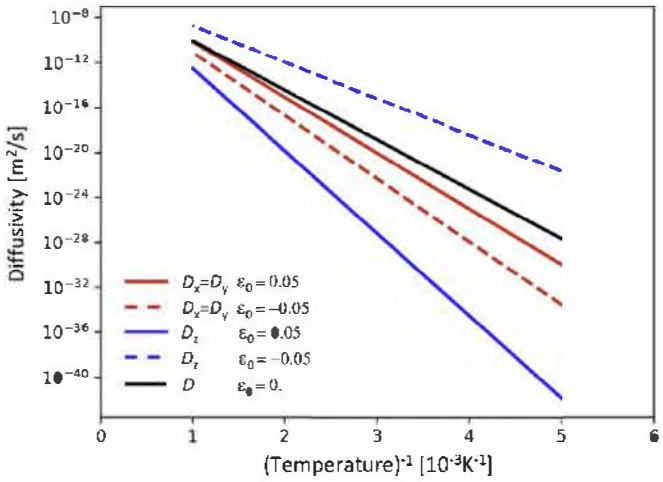

Fig. 6. Arrhenius plot of diffusivities for axial strains $\boldsymbol{\varepsilon} = (0, 0, \pm 0.05)$. The activation energies depend on the direction of diffusion and on the strain level. The black line is the reference cubic ferrite.

were derived.

Fig. 7 illustrates the influence of carbon content on diffusion in the reference case of a stress-free crystal at room temperature:

1) Below the transition composition of $c_0 = 0.0125$, the order parameter remains null in ferrite (Fig. 7a). The lattice strain increases linearly with composition on account of the relaxation volume of carbon. Correlatively, the migration enthalpy increases and the diffusivity in ferrite slowly decreases with carbon content.
2) At the transition, the order parameter jumps from 0 to 0.5 as cubic ferrite transforms into tetragonal martensite. Due to the change of crystal symmetry, all variables split into new values, and the diffusivities undergo sharp discontinuities.
3) Above the transition composition, the order parameter grows continuously towards 1. Crystal volume and tetragonality increase continuously. All diffusivities decrease with increasing carbon content, but transverse diffusivity remains dominant.

These results show that room-temperature carbon diffusivity in stress-free martensite is highly anisotropic and is dominated by diffusion perpendicular to the axis of tetragonality.

Fig. 8 summarizes the behavior of the diffusivity D at room temperature as function of composition in the case of an axial stress $\boldsymbol{\sigma} = (0, 0, \sigma_0)$. The agreement between KMC simulations (points) and elastodiffusion model (lines) is better than one percent in most cases. The absence of KMC results at $c = 0.013$ and 0.015 for $\sigma_0 = -100$ MPa is due instabilities of the tetragonal crystal under compressive stress. This topic will be discussed in a future publication.

Tension in the axial direction stabilizes Zener ordering (Fig. 8a). On the contrary, axial compression stabilizes inverse-Zener ordering when c is smaller than the coexistence value. At the composition of coexistence, the discontinuity in order parameter produces a discontinuity in diffusivity: an upward jump when $\sigma_0 > 0$, and a drop when $\sigma_0 < 0$. As mentioned in Sec. 2, when σ_0 is larger than the room-temperature critical stress of 11.5 MPa, the order parameter varies continuously with carbon content. In this case, a change of slope in the diffusivity occurs in the vicinity of the transition region, *i.e.* around $\eta = 0.25$. Far from the transition region, the slopes are dominated by one of the migration enthalpies, as discussed in Sec. 3, and $\ln D$ tends to a linear function of carbon content.

Far from the transition region, the diffusivities are arrhenian in ferrite and in martensite, but with different, stress-dependent, activation energies (Fig. 9). For each stress level lower than the critical stress, a discontinuity is observed at the temperature of transition. Axial diffusivity is found more sensitive to temperature change than transverse diffusivity.

5. Discussion

We found that the diffusivities of carbon atoms in bcc- and bct-iron are sensitive to the mechanical loading of the crystal. In the case of tetragonal loading, axial and transverse diffusivity may

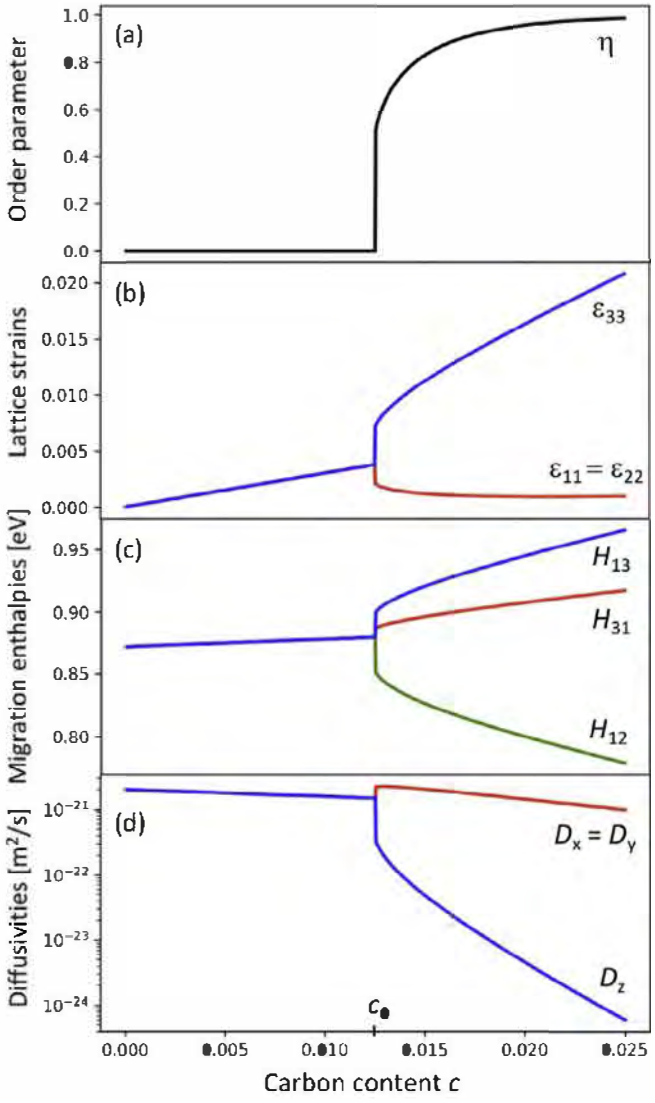

Fig. 7. (a) Order parameter, (b) lattice strains, (c) migration enthalpies and (d) corresponding diffusivities of carbon, as function of carbon content in stress-free bcc-iron ($c < c_0$) and bct-iron ($c > c_0$) at room temperature (293 K).

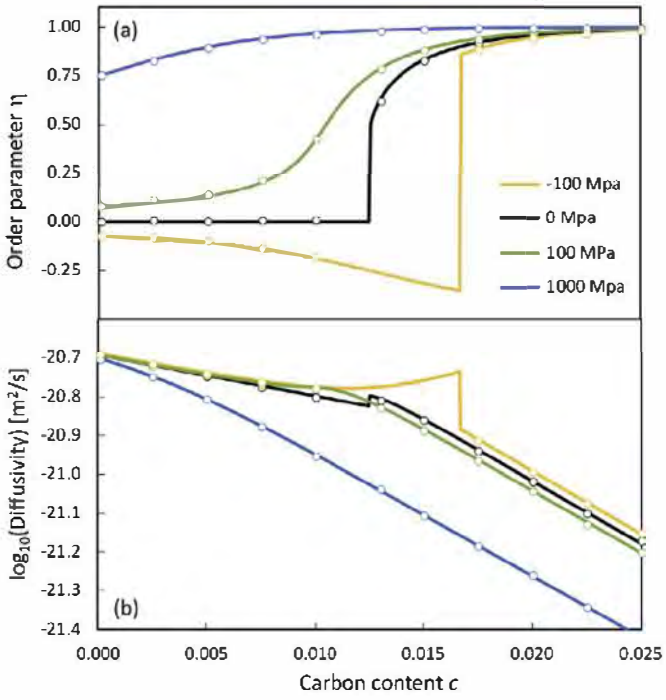

Fig. 8. (a) Order parameter η and (b) diffusivity D at $T = 293$ K as function of carbon content, for various axial stresses. KMC simulations (points) and elastodiffusion model (lines).

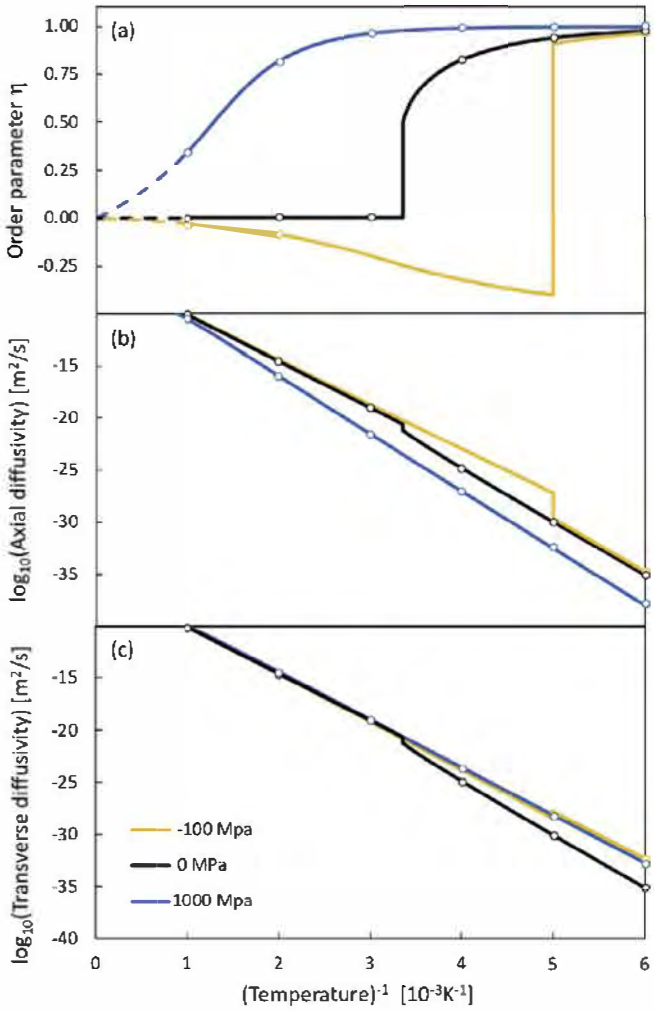

Fig. 9. Axial and transverse diffusivities D_z and D_x at $c = 1.235\%$ as function of temperature, for various axial stresses. KMC simulations (points) and elastodiffusion model (lines).

differ by several orders of magnitude, exhibiting a largely anisotropic behavior. Anisotropy is intrinsic to stress-free martensite since martensite is itself a tetragonally deformed crystal.

Our analytical results are supported by comparison with KMC simulations in both deformed ferrite and martensite. The numerical results are limited to the accuracy of the material parameters in use, and especially those derived from DFT calculations. The uncertainty on the stiffness constants and the dipole tensor components can reasonably be estimated to about 20% in the range of composition and temperature under interest. Under these conditions, our conclusions remain largely valid.

Few literature studies have been dedicated to carbon diffusivity in supersaturated iron. Some are limited to fully ordered martensite [22,27]; others incorporate the effect of partial ordering [50]. Diffusion anisotropy, slowing-down by Zener ordering and effect of pressure can be compared quantitatively.

1) From Eq. (8), in stress-free fully ordered martensite ($\eta = 1$, $\boldsymbol{\sigma} = \mathbf{0}$), the strain components write numerically as function of composition c

$$\begin{aligned} \varepsilon_{11} &= \varepsilon_{22} = 0.0364\, c \\ \varepsilon_{33} &= 0.840\, c. \end{aligned} \tag{27}$$

These values are in good agreement with the experimental review of Chen et al. [51], as reported in Ref. [26]. From Eq. (11), the corresponding variations in migration enthalpies $H_{ij} - H_0^{\mathrm{m}}$ are

$$\begin{aligned} \Delta H_{12} &= -3.81c \\ \Delta H_{13} &= +3.77c \\ \Delta H_{31} &= +1.82c \end{aligned} \tag{28}$$

with $H_0^{\mathrm{m}} = 0.872$ eV. On their side, by molecular dynamics with EAM potential coupled to kinetic Monte Carlo, Lawrence et al. [27] found

$$\begin{aligned} \Delta H_{12} &= -1.87x_{\mathrm{C}} \\ \Delta H_{13} &= -1.17x_{\mathrm{C}} \\ \Delta H_{31} &= +1.13x_{\mathrm{C}} \end{aligned} \tag{29}$$

with $H_0^{\mathrm{m}} = 0.815$ eV and $x_{\mathrm{C}} = c/(1+c)$. Eqs. (28) and (29) agree that the migration enthalpy H_{12} is the lowest of the three, *i.e.* the jumps from disfavored to favored sites are the most probable in stress-free martensite. However, the values differ in magnitude. Eqs. (29) also state that axial migration enthalpy is favored ($\Delta H_{13} < 0$). As a consequence, the data of Lawrence et al. predict diffusion channeling along the axis of tetragonality. Our findings are at variance. Indeed, from Eq. (26) the anisotropy ratio in fully-ordered martensite writes

$$\frac{D_z}{D_x} = \left(\frac{a_z}{a_x}\right)^2 \exp\left[-\frac{7.57\, c}{k_{\mathrm{B}}T}\right]. \tag{30}$$

The positive activation energy of the ratio (7.57 c in eV) implies strong transverse diffusion in stress-free martensite: at room temperature, the ratio equals 0.113 for $c = 0.0125$. It reaches 5.4×10^{-17} for $c = 0.125$, *i.e.* no axial diffusion is to be expected in the compound $Fe_{16}C_2$.

2) Hillert [22] was the first to suggest that carbon-induced tetragonality would slow down carbon diffusion in martensite. He argued that carbon diffusivity is controlled by the jump frequency out of the favored octahedral sites, *i.e.* Γ_{31} with our notations. Our analysis confirms this intuition, since $D \approx \frac{2}{3}(a_x^2/2)\Gamma_{31}$ in case of positive tetragonality (see Sec. 3). Using the data of Zener [3], Hillert approximated the change in activation energy to $E_{\mathrm{HZ}} = 3.11$ eV per unit carbon fraction. From our model, we find $E_{\mathrm{HZ}} = 1.82$ eV with our materials data [Eq. (28)], and 1.13 eV with the data of Lawrence et al. [Eq. (29)]. The value of Hillert suffers from a rough approximation of the activation energy formulation, due to the lack of appropriate data about the tetrahedral sites. Lawrence's value is smaller than ours because the lattice tetragonality is underestimated by their EAM potential. Accurate experimental investigation of the carbon diffusivity in supersaturated iron is still missing. However, indirect determination was recently made available: using a kinetic model of spinodal decomposition of virgin Fe-Ni-C martensite, E_{HZ} was fitted to 4 eV [18]. This value is relatively close to the activation enthalpy of the present work $\Delta H_{13}/c = 3.77$ eV, suggesting that diffusion in the axial direction is the limiting mechanism for spinodal decomposition. This is in accordance with the recent theoretical investigation of Yan et al. [15], who exhibited decomposition of martensite into a modulated structure of wave vector [0 0 ξ_0] parallel to the applied strain, hence necessitating diffusion in the axial direction.

3) The effect of pressure on the diffusivities is dictated by the value of $\Delta P = \mathrm{tr}(\mathbf{P}^{T} - \mathbf{P}^{O})$ [Eq. (23)], or equivalently by the activation volume $\Delta V = (S_{11} + 2S_{12})\Delta P$. The sign of ΔP is sensitive to the exact value of the components of the dipole tensors $\mathbf{P}^{T}$ and $\mathbf{P}^{O}$. Our DFT calculations and those of Souissi et al. [31] yield $\Delta P < 0$, whereas the EAM potential [27] yields $\Delta P > 0$ (Table 3). Hence, our results predict an increase in diffusivity with increased pressure (or decreased volume), whereas Lawrence data [27] predict the opposite. Given the experimental uncertainties, the scarce measurements of the activation volume at low temperature do not allow concluding on this point (see Table 3) [19,20].

An indirect effect of the activation volume can be computed via the linear thermal expansion coefficient $\alpha(T)$: when substituted in Eq. (23), the thermal strain $\varepsilon^{th} = \int \alpha(T)\mathrm{d}T$ yields the expansion-induced variation in migration energy. This, in principle, produces a deviation from the Arrhenius law. Using the data of [52], we find a decrease in diffusivity by a factor of 0.75 at the ferrite − austenite transition temperature ($T = 1185$ K). Contrary to Lawrence, we conclude that this effect is too small to explain the deviations from arrhenian behavior that one may see in the data compiled by da Silva et al. [45] or Weller [53].

Our results show that the magnitude of carbon diffusivity in ferrite and martensite is sensitive to the magnitude and orientation of the stress or strain. The effects can be large when the strain is of the order of a few percent. Such levels of lattice strain can be reached in supersaturated martensite or in heavily deformed ferrite. In these situations, the anisotropy of diffusion will favor anisotropic microstructure formation. For example, the first stages of spinodal decomposition of virgin martensite are possibly driven by the anisotropy of diffusion. If so, carbide lamellae will form perpendicular to the axis of fast diffusion. Alternatively, if the morphology is driven by elastic energy more than by diffusion, the kinetics of decomposition will be largely affected by sluggish diffusion in some crystallographic directions, depending on the local magnitude and direction of the strains. Similarly, the anisotropy of diffusion is likely to play a role in the kinetics of coarsening of cementite lamellae in highly deformed cold-drawn perlite [54].

To go further, by controlling the direction and magnitude of the strain and/or stress field, the morphology of carbide lamellae formed in supersaturated martensite may be driven: uniaxial compression is expected to favor lamellae perpendicular to the (fast diffusing) axial direction, whereas uniaxial traction would favor lamellae in zone axis with the axial direction, in analogy to the strain-induced rafting phenomenon in Ni-based superalloys [55]. Control of such mechanisms opens the way to strain or stress "engineering" of martensite in the future.

6. Conclusions

We developed a model for the diffusivity of carbon atoms in bct-iron, including ferrite and martensite phases in a coherent approach. The model is based on the anisotropic linear elasticity theory of point defects, the dilute approximation of regular solutions and the multisite model of random walk. It allows predicting the effects of composition, temperature and mechanical loading on the anisotropy of carbon diffusion in bct-iron.

We showed that tracer diffusion of carbon in ferrite is sensitive to the mechanical loading: axial expansion/tension favors transverse diffusion, whereas axial contraction/compression favors axial diffusion. The channeling effect in the axial direction can be very strong for strains of a few percent, commonly encountered in martensite.

Diffusion in stress-free martensite depends not only on carbon content but also on the degree of Zener ordering. Carbon diffusion is highly anisotropic and is dominated by migration perpendicular to the axis of tetragonality. The diffusivity is significantly reduced in highly supersaturated martensite.

Diffusion in stressed martensite is generally accelerated by axial compression and slowed down by axial tension. It exhibits a complex behavior as function of composition and temperature in the vicinity of the martensite − ferrite transition, and a discontinuity at the transition.

These results suggest that the kinetics of carbon ordering in stressed bct-iron microstructures is very sensitive to the local state of strain/stress of the crystals. Also, the microstructure of martensite is expected to be affected by stresses applied during thermal ageing. Such phenomena could be exploited for "stress engineering" of ferrous martensitic alloys.

Table 3
Isotropic part of the dipole tensor of migration ΔP, and volume of migration ΔV. Comparison with data extracted from the literature.

	ΔP (eV)	ΔV (Å^3)
This work (DFT)	−2.03	−0.58
Souissi (DFT) [25,31]	−2.66	−0.75[a]
Lawrence (EAM) [27]	4.97	1.49[a]
Bosman (exp.) [19]		-0.07 ± 0.07
Bass (exp.) [20]		0.0 ± 0.2

[a] Calculated from ΔP and the elastic constants.

Acknowledgements

The Agence Nationale de la Recherche (contract SPIDERMAN 13-BS08-0014-02) is thanked for its financial support. All atom visualizations were performed using Ovito software [56].

References

[1] D. a. Porter, K.E. Easterling, Phase Transformations in Metals and Alloys, Chapman & Hall, 1992, https://doi.org/10.1007/978-1-4899-3051-4.
[2] R. Rementeria, J.A. Jimenez, S.Y.P. Allain, G. Geandier, J.D. Poplawsky, W. Guo, et al., Quantitative assessment of carbon allocation anomalies in low temperature bainite, Acta Mater. 133 (2017) 333–345, https://doi.org/10.1016/j.actamat.2017.05.048.
[3] C. Zener, Theory of strain interaction of solute atoms, Phys. Rev. 74 (1948) 639–647, https://doi.org/10.1103/PhysRev.74.639.
[4] M.J. Genderen, M. Isac, a. Böttger, E.J. Mittemeijer, Aging and tempering behavior of iron-nickel-carbon and iron-carbon martensite, Metall. Mater. Trans. A. 28 (1997) 545–561, https://doi.org/10.1007/s11661-997-0042-5.
[5] L.S. Darken, R.W. Gurry, Physical Chemistry of Metals, McGraw-Hill Book Company Inc., New York Toronto London, 1953.
[6] P. Maugis, Ferrite, martensite and supercritical iron: a coherent elastochemical theory of stress-induced carbon ordering in steel, Acta Mater. 158 (2018) 454–465, https://doi.org/10.1016/J.ACTAMAT.2018.08.001.
[7] A.G. Khachaturyan, G.A. Shatalov, On the theory of the ordering of carbon atoms in a martensite crystal, Fiz. Met. Met. 32 (1971) 1–9.
[8] G.V. Kurdjumov, A.G. Khachaturyan, Nature of axial ratio anomalies of the martensite lattice and mechanism of diffusionless gamma to alpha transformation, Acta Metall. 23 (1975) 1077–1088, https://doi.org/10.1016/0036-9748(75)90354-3.
[9] L. Xiao, Z. Fan, Z. Jinxiu, Z. Mingxing, K. Mokuang, G. Zhenqi, Lattice-parameter variation with carbon content of martensite. I. X-ray-diffraction experimental study, Phys. Rev. B 52 (1995) 9970–9978.
[10] Z. Fan, L. Xiao, Z. Jinxiu, K. Mokuang, G. Zhenqi, Lattice-parameter variation with carbon content of martensite. II. Long-wavelength theory of the cubic-to-tetragonal transition, Phys. Rev. B 52 (1995) 9979–9987.
[11] C.W. Sinclair, M. Perez, R.G.A. Veiga, A. Weck, Molecular dynamics study of the ordering of carbon in highly supersaturated alpha-Fe, Phys. Rev. B 81 (2010), 224204, https://doi.org/10.1103/PhysRevB.81.224204.
[12] S. Djaziri, Y. Li, G.A. Nematollahi, B. Grabowski, S. Goto, C. Kirchlechner, et al., Deformation-induced Martensite : a new paradigm for exceptional steels, Adv. Mater. 28 (2016) 7753–7757, https://doi.org/10.1002/adma.201601526.
[13] G.A. Nematollahi, B. Grabowski, D. Raabe, J. Neugebauer, Multiscale description of carbon-supersaturated ferrite in severely drawn pearlitic wires, Acta Mater. 111 (2016) 321–334, https://doi.org/10.1016/j.actamat.2016.03.052.
[14] P.V. Chirkov, A.A. Mirzoev, D.A. Mirzaev, Role of stresses and temperature in the Z ordering of carbon atoms in the martensite lattice, Phys. Met. Metallogr.

117 (2016) 1138–1143, https://doi.org/10.1134/S0031918X16110041.
[15] J.Y. Yan, A.V. Ruban, Configurational thermodynamics of C in body-centered cubic/tetragonal Fe: a combined computational study, Comput. Mater. Sci. 147 (2018) 293–303, https://doi.org/10.1016/j.commatsci.2018.02.024.
[16] K.A. Taylor, M. Cohen, Ageing of ferrous martensites, Prog. Mater. Sci. 36 (1992) 225–272.
[17] N. DeCristofaro, R. Kaplow, W.S. Owen, The kinetics of carbon clustering in martensite, Metall. Trans. A. 9 (1978) 821–825, https://doi.org/10.1007/BF02649791.
[18] P. Maugis, F. Danoix, M. Dumont, S. Curelea, S. Cazottes, H. Zapolsky, et al., Carbon diffusivity and kinetics of spinodal decomposition of martensite in a model Fe-Ni-C alloy, Mater. Lett. 214 (2018) 213–216, https://doi.org/10.1016/j.matlet.2017.12.007.
[19] A.J. Bosman, P.E. Brommer, L.C.H. Eijkelenboom, C.J. Schinkel, G.W. Rathenau, The influence of pressure on the mean time of stay of interstitial carbon in iron, Physica 26 (1960) 533–538. https://doi.org/10.1016/0031-8914(60)90105-1.
[20] J. Bass, D. Lazarus, Effect of pressure on mobility of interstitial carbon in iron, J. Phys. Chem. Solid. 23 (1962) 1820–1821.
[21] R.A. Johnson, Calculation of the energy and migration characteristics of carbon in martensite, Acta Metall. 13 (1965) 1259–1262, https://doi.org/10.1016/0001-6160(65)90035-0.
[22] M. Hillert, The kinetics of the first stage of tempering, Acta Metall. 7 (1959) 653–658, https://doi.org/10.1016/0001-6160(59)90141-5.
[23] U. Landman, M.F. Shlesinger, Stochastic theory of multistate diffusion in perfect and defective systems. II. Case studies, Phys. Rev. B 19 (1979) 6220–6237, https://doi.org/10.1103/PhysRevB.19.6220.
[24] U. Landman, M.F. Shlesinger, Stochastic theory of multistate diffusion in perfect and defective systems. I. Mathematical formalism, Phys. Rev. B 19 (1979) 6207–6219.
[25] M. Souissi, H. Numakura, Elastic properties of Fe–C and Fe–N martensites, ISIJ Int. 55 (2015) 1512–1521, https://doi.org/10.2355/isijinternational.55.1512.
[26] S. Chentouf, S. Cazottes, F. Danoix, M. Goune, H. Zapolsky, P. Maugis, Effect of interstitial carbon distribution and nickel substitution on the tetragonality of martensite: a first-principles study, Intermetallics 89 (2017) 92–99, https://doi.org/10.1016/j.intermet.2017.05.022.
[27] B. Lawrence, C.W. Sinclair, M. Perez, Carbon diffusion in supersaturated ferrite : a comparison of mean-field and atomistic predictions, Model. Simulat. Mater. Sci. Eng. 22 (2014) 1–17, https://doi.org/10.1088/0965-0393/22/6/065003.
[28] P. Maugis, F. Danoix, H. Zapolsky, S. Cazottes, M. Gouné, Temperature hysteresis of the order-disorder transition in carbon-supersaturated α-Fe, Phys. Rev. B 96 (2017), 214104, https://doi.org/10.1103/PhysRevB.96.214104.
[29] J.F. Nye, Physical Properties of Crystals, Clarendon Press, Oxford, 1985.
[30] C. Varvenne, E. Clouet, Elastic dipoles of point defects from atomistic simulations, Phys. Rev. B 96 (2017), 224103, https://doi.org/10.1103/PhysRevB.96.224103.
[31] M. Souissi, Y. Chen, M.H.F. Sluiter, H. Numakura, Ab initio characterization of B, C, N, and O in bcc iron: solution and migration energies and elastic strain fields, Comput. Mater. Sci. 124 (2016) 249–258, https://doi.org/10.1016/j.commatsci.2016.07.037.
[32] D.J. Bacon, D.M. Barnett, R.O. Scattergood, Anisotropic continuum theory of lattice defects, Prog. Mater. Sci. 23 (1980) 51, https://doi.org/10.1016/0079-6425(80)90007-9.
[33] R.W. Balluffi, Introduction to Elasticity Theory for Crystal Defects, Cambridge University Press, 2012, https://doi.org/10.1017/CBO9780511998379.
[34] S. Nagakura, Y. Hirotsu, M. Kusunoki, T. Suzuki, Y. Nakamura, Crystallographic study of the tempering of martensitic carbon steel by electron microscopy and diffracion, Metall. Trans. A. 14A (1983) 1025–1031.
[35] O.D. Sherby, J. Wadsworth, D.R. Lesuer, C.K. Syn, The c/a ratio in quenched Fe-C and Fe-N steels - a heuristic story, Mater. Sci. Forum 539–543 (2007) 215–222, doi:10.4028/www.scientific.net/MSF.539-543.215.
[36] M. David, D. Connétable, Diffusion of interstitials in metallic systems, illustration of a complex study case: aluminum, J. Phys. Condens. Matter 29 (2017), 455703, https://doi.org/10.1088/1361-665X/aa722d.
[37] J. Philibert, Atom Movements, Diffusion and Mass Transport in Solids, Editions de physique, 1991.
[38] G. Kresse, J. Hafner, Ab initio molecular dynamics for liquid metals, Phys. Rev. B 47 (1993) 558. LP-561.
[39] G. Kresse, D. Joubert, From ultrasoft pseudopotentials to the projector augmented-wave method, Phys. Rev. B 59 (1999) 1758–1775.
[40] J.P. Perdew, K. Burke, M. Ernzerhof, Generalized gradient approximation made simple, Phys. Rev. Lett. 78 (1997) 1396.
[41] H.J. Monkhorst, J.D. Pack, Special points for Brillouin-zone integrations, Phys. Rev. B 13 (1976) 5188–5192, https://doi.org/10.1103/PhysRevB.13.5188.
[42] A. Togo, I. Tanaka, First principles phonon calculations in materials science, Scr. Mater. 108 (2015) 1–5, https://doi.org/10.1016/J.SCRIPTAMAT.2015.07.021.
[43] H. Eyring, The activated complex in chemical reactions, J. Chem. Phys. 3 (1935) 107–115, https://doi.org/10.1063/1.1749604.
[44] K. Tapasa, A.V. Barashev, D.J. Bacon, Y.N. Osetsky, Computer simulation of carbon diffusion and vacancy-carbon interaction in alpha-iron, Acta Mater. 55 (2007) 1–11, https://doi.org/10.1016/j.actamat.2006.05.029.
[45] J.R.G. da Silva, R.B. McLellan, Diffusion of carbon and nitrogen in B.C.C. iron, Mater. Sci. Eng. 26 (1976) 83–87, https://doi.org/10.1016/0025-5416(76)90229-9.
[46] D. Gendt, P. Maugis, G. Martin, M. Nastar, F. Soisson, Monte Carlo simulation of NbC precipitation kinetics in alpha-Fe, Defect Diffusion Forum 194–199 (2001) 1779–1786, https://doi.org/10.4028/www.scientific.net/DDF.194-199.1779.
[47] C. Hin, Y. Bréchet, P. Maugis, F. Soisson, Kinetics of heterogeneous dislocation precipitation of NbC in alpha-iron, Acta Mater. 56 (2008) 5535–5543, https://doi.org/10.1016/j.actamat.2008.07.044.
[48] C. Hin, Y. Bréchet, P. Maugis, F. Soisson, Kinetics of heterogeneous grain boundary precipitation of NbC in alpha-iron: a Monte Carlo study, Acta Mater. 56 (2008) 5653–5667.
[49] W.M. Young, E.W. Elcock, Monte Carlo studies of vacancy migration in binary ordered alloys: I, Proc. Phys. Soc. 89 (1966) 735–746, https://doi.org/10.1088/0370-1328/89/3/329.
[50] D.R. Trinkle, Diffusivity and derivatives for interstitial solutes: activation energy, volume, and elastodiffusion tensors, Philos. Mag. A 96 (2016) 2714–2735, https://doi.org/10.1080/14786435.2016.1212175.
[51] L. Cheng, A. Bottger, T.H. de Keijser, E.J. Mittemeijer, Lattice parameters of iron-carbon and iron-nitrogen martensites and austenites, Scr. Metall. Mater. 24 (1990) 509–514.
[52] Y.S. Touloukian, R.K. Kirby, R.E. Taylor, P.D. Desai, Thermophysical Properties of Matter - the TPRC Data Series, in: Thermal Expansion Metallic Elements and Alloys, vol. 12, Plenum press, New York, 1975, https://doi.org/10.1007/978-1-4757-1622-1.
[53] M. Weller, Anelastic relaxation of point defects in cubic crystals, Le J. Phys. IV (06) (1996), https://doi.org/10.1051/jp4:1996812. C8-63-C8-72.
[54] J. Languillaume, G. Kapelski, B. Baudelet, Cementite dissolution in heavily cold drawn pearlitic steel wires, Acta Mater. 45 (1997) 1201–1212, https://doi.org/10.1016/S1359-6454(96)00216-9.
[55] M. Kamaraj, Rafting in single crystal nickel-base superalloys — an overview, Sadhana 28 (2003) 115–128, https://doi.org/10.1007/BF02717129.
[56] A. Stukowski, Visualization and analysis of atomistic simulation data with OVITO–the Open Visualization Tool, Model. Simulat. Mater. Sci. Eng. 18 (2010), 015012, https://doi.org/10.1088/0965-0393/18/1/015012.